

Highly Accelerated Dynamic Contrast Enhanced Imaging

Robert Marc Lebel,^{1*†} Jesse Jones,² Jean-Christophe Ferre,² Meng Law,²
and Krishna S. Nayak¹

Purpose: Dynamic contrast-enhanced imaging provides unique physiological information, notably the endothelial permeability (K^{trans}), and may improve the diagnosis and management of multiple pathologies. Current acquisition methods provide limited spatial-temporal resolution and field-of-view, often preventing characterization of the entire pathology and precluding measurement of the arterial input function. We present a method for highly accelerated dynamic imaging and demonstrate its utility for dynamic contrast-enhanced modeling.

Methods: We propose a novel Poisson ellipsoid sampling scheme and enforce multiple spatial and temporal l_1 -norm constraints during image reconstruction. Retrospective and prospective analyses were performed to validate the approach.

Results: Retrospectively, no mean bias or diverging trend was observed as the acceleration rate was increased from $3\times$ to $18\times$; less than 10% error was measured in K^{trans} at any individual rates in this range. Prospectively accelerated images at a rate of $36\times$ enabled full brain coverage with $0.94 \times 0.94 \times 1.9 \text{ mm}^3$ spatial and 4.1 s temporal resolutions. Images showed no visible degradation and provided accurate K^{trans} values when compared to a clinical population.

Conclusion: Highly accelerated dynamic MRI using compressed sensing and parallel imaging provides accurate permeability modeling and enables full brain, high resolution acquisitions. *Magn Reson Med* 71:635–644, 2014. © 2013 Wiley Periodicals, Inc.

Key words: magnetic resonance imaging; compressed sensing; parallel imaging; dynamic imaging; contrast enhanced; sparsity; undersampling

Dynamic contrast-enhanced (DCE) MRI employs serial T_1 -w imaging, typically with a three-dimensional (3D) spoiled gradient echo sequence, during a bolus injection of a Gadolinium-based contrast agent. Changes in signal intensity are mapped to changes in contrast agent concentration then regressed to quantify physiological parameters related to vascular permeability (K^{trans} , K_{ep}) and cellular compartmentalization volumes, including the fractional plasma volume (v_p) and the extravascular-extracellular volume fraction (v_e) (1,2).

DCE is a promising tool for tumor assessment as it enables quantification of vascular and cellular irregularities. Histologically, abnormal blood–brain barrier permeability is associated with tumor progression; this is observed with DCE imaging, where K^{trans} correlates with tumor grade (3). It has been used for monitoring therapy response (4) and holds vast potential for drug trials (5). Despite unequivocal benefits, clinical and research adoption has been limited. This is due, in part, to suboptimal image acquisition.

Acquisition of imaging data for DCE is challenging since a new image volume must be obtained every 1–30 s to detect signal intensity changes resulting from diffusion of the agent from the intravascular space to the extravascular-extracellular space (6–8). As a result, spatial resolution and volume coverage are severely restricted. A typical protocol is limited to ~ 2000 repetition periods, with data distributed across the phase- and slice-encodes. In-plane resolution typically exceeds 1 mm^2 and slices are often at least 5 mm thick. Despite thick slices, volume coverage is frequently inadequate to cover the known pathology; previously unknown pathologies are likely missed. Additionally, limited volume coverage and spatial-temporal resolution precludes consistent, patient-specific, extraction of the arterial input function (AIF), which is important for accurate pharmacokinetic modeling (9). Methods to reconstruct images from vastly undersampled data are predicted to improve DCE imaging (10).

Parallel imaging (PI) enables slightly accelerated image acquisition. Modest acceleration rates can often be achieved with tolerable noise amplification and residual aliasing artifacts. Unfortunately, limited slice coverage precludes substantial acceleration in the slice-encode direction. Traditional data sharing methods, such as TRICKS (11) or TWIST (12), sample the center of k -space more frequently than the periphery and allow accelerated acquisitions at the expense of spatial-frequency dependent temporal blurring. PI and conventional data sharing has become standard in many DCE protocols, but full volume coverage with high spatial-temporal resolution remains elusive.

Recently, compressed sensing (CS) has been shown to relax the MRI sampling requirements (13), enabling accelerated acquisitions. This approach applies reconstruction constraints to undersampled data to synthesize an image. It iteratively minimizes coefficients in a sparse representation to suppress unwanted features while maintaining those consistent with the acquired data. Efficacy hinges on the sparsity transform(s); representations requiring few non-zero coefficients can be highly accelerated. In general, sparsity is enhanced with the dimensionality of the application, making 4D dynamic acquisitions amenable to acceleration via CS.

¹Ming Hsieh Department of Electrical Engineering, Viterbi School of Engineering, University of Southern California, Los Angeles, California, USA.

²Department of Radiology, Keck School of Medicine, University of Southern California, Los Angeles, California, USA.

*Correspondence to: R. Marc Lebel, Ph.D., Seaman Family MR Research Centre, Foothills Medical Centre, Calgary, Canada. E-mail: mlebel@gmail.com

[†]Current address: GE Healthcare, Calgary, Canada

Received 20 August 2012; revised 24 January 2013; accepted 30 January 2013

DOI 10.1002/mrm.24710

Published online 15 March 2013 in Wiley Online Library (wileyonlinelibrary.com).

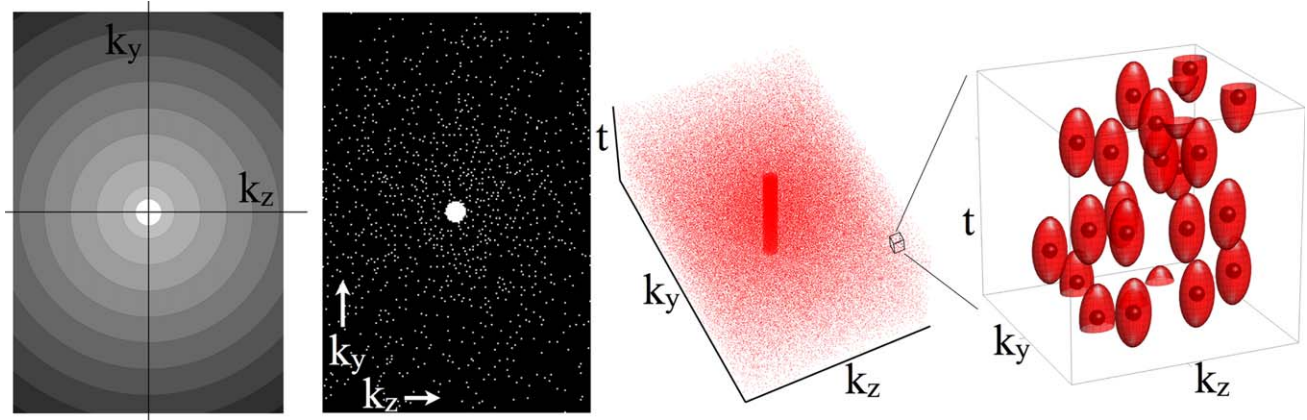


FIG. 1. Variable density Poisson ellipsoid sampling scheme for dynamic 3D acquisitions. **a**: Variable sampling density in k_y - k_z space is achieved by dividing k -space into annuli with radially decreasing sampling densities. During computation, subsequent samples are placed in the annuli furthest from its target density. **b**: The resulting sampling pattern (white locations are acquired locations; black are omitted) has a fully sampled center with a higher sampling density near the center of k -space than at the periphery. **c**: Dynamic sampling tables are obtained by defining hypothetical ellipsoids in k - t space [shown in **(d)**], which define volumes that exclude subsequent sampling. Sample locations are chosen pseudo-randomly, constrained to avoid proximity to other samples and to fulfill the annular sampling density. [Color figure can be viewed in the online issue, which is available at wileyonlinelibrary.com]

To date, several works have employed CS (or similar approaches) for DCE imaging. Notably, Adluru et al. (14) employed a nonlocal means constraint to reconstruct $5\times$ retrospectively undersampled DCE data. Chen et al. (15) proposed a temporally constrained reconstruction and demonstrated accurate pharmacokinetic modeling at a retrospective acceleration rate of $6\times$. Smith et al. (16,17) demonstrated retrospective acceleration between $2\times$ and $4\times$ and reported generally accurate K^{trans} values but some inconsistency was observed between human and animal studies. Han et al. (18) implemented an $8\times$ prospectively accelerated 2D method with spatial and temporal constraints and demonstrated a correlation between accelerated and fully sampled data. To the best of our knowledge, no one has effectively combined PI and CS for prospectively accelerated DCE imaging nor fully characterized the resulting errors in the pharmacokinetic modeling endpoints.

In this work, we describe a novel data sampling strategy and reconstruction constraints to leverage both PI and CS to enable highly accelerated dynamic acquisitions and accurate DCE imaging. We validate the accuracy of this method with a retrospective analysis of fully sampled image sets and demonstrate its utility for prospectively accelerated high resolution, full brain DCE MRI. The proposed accelerated protocol provides full brain coverage with $0.94 \times 0.94 \times 1.9 \text{ mm}^3$ spatial- and 4.1 s temporal-resolution.

METHODS

Variable Density Poisson Ellipsoid Sampling

Poisson disc sampling balances uniform and random sample spacing and is suitable for combined PI and CS (19). This approach defines a set of phase- and slice-

encodes, chosen stochastically from Cartesian k_y - k_z space (the readout, k_x , is fully sampled) with the constraint that samples not coexist within discs surrounding each sample. Here, we modify this approach to enable variable density sampling, and extend it for dynamic imaging with 3D volumes, Figure 1.

Variable density (Fig. 1a) is achieved by subdividing k_y - k_z space into a series of i annuli with interior radii r_i . Each annulus is assigned a uniform sampling density ρ_i that decreases exponentially from the center of k -space with a decay constant τ ,

$$\rho_i = \rho_0 e^{-r_i/\tau}. \quad [1]$$

The scaling factor ρ_0 is chosen to ensure that the total number of sampled points (based on the matrix size and acceleration rate), n_t , are acquired. With this scaling, the number of desired samples per annulus, n_i , is given by

$$n_i = n_t \frac{N_i e^{-r_i/\tau}}{\sum_i N_i e^{-r_i/\tau}}. \quad [2]$$

where N_i is the number of possible sampling locations within an annulus (readily computed numerically). In this work, we employed a decay constant of 3 cm^{-1} , chosen empirically for relatively high sampling density in the center and non-zero density at the periphery of k -space. We enforce a fully sampled central region containing 10% of the total samples—these samples are not subject to the minimum spacing requirements of Poisson disc sampling.

Dynamic sampling was achieved by extending the conceptual k_y - k_z discs surrounding each sample into k_y - k_z - t ellipsoids, Figure 1c,d. These ellipsoids define the minimum distance between samples and determine the amount of uniformity and randomness in the sampling

pattern. Ellipsoid radii (independent of radii used for variable sampling density) in the k_y and k_z directions were chosen based on the PI capabilities of the receiver array. All data were acquired with an eight-channel head coil—suitable for PI in the anterior/posterior and left/right directions. Retrospective images were acquired in the axial plane and the k_y and k_z radii were nominally set to 3.0 and 0.75 samples respectively while the temporal radius was set at three time frames. The k_y radius was reduced to two points at $9\times$, $12\times$, and $15\times$ and to one point at $3\times$ and $6\times$ to accommodate the required sampling density. Prospectively undersampled images were acquired coronally, enabling 2D PI. In this case, radii of two points, two points, and two frames were employed in the k_y , k_z , and time dimensions respectively.

Sampling tables were computed with a dart-throwing algorithm, governed by the following pseudo-code:

Define τ , r_i 's, and Poisson ellipsoid radii
Compute n_t , ρ_o , ρ_v , N_i 's, n_i 's

Initialize empty list of defined sample locations
WHILE (length of defined sample locations $< n_t$)

Determine time frame for a candidate sample location
(from frames with the fewest samples)

Determine radial bounds for a candidate sample location
(annulus furthest from its target density)

Randomly determine candidate k_y - k_z - t location within
radial and temporal bounds

IF (candidate location is not within the Poisson ellipsoid
of any defined sample location)

Concatenate candidate location to defined sample
locations

ENDIF

ENDWHILE

Append fully sampled central locations to defined
sample locations

Constrained Reconstruction

Images were reconstructed using a sparse SENSE signal model (20,21) with multiple spatial and temporal constraints, applied as l_1 -norm penalties, to reconstruct the 4D data sets. Multiple penalties were employed to lessen the burden on individual constraints, minimizing compression artifacts characteristic of each transform. The image, m (in vector form), was obtained by minimizing

$$f(m) = \|\mathbf{F}_u \mathbf{S} m - y\|_2^2 + \lambda_1 \|\mathbf{V} m\|_1 + \lambda_2 \|\Psi m\|_1 + \lambda_3 \|\mathbf{T}_v m\|_1 \quad [3]$$

where \mathbf{F}_u is the undersampled Fourier operator, \mathbf{S} is the sensitivity operator, y is the acquired k-space data, \mathbf{V} is a temporal high-pass filter, Ψ is a 4D wavelet transform, and \mathbf{T}_v is total variation in the spatial domain. These constraints are described in more detail in the following section. An initial estimate of m was obtained via temporally averaged data. The initial image estimate was scaled to a maximum value of 1; this scale factor was also applied to y . Selection of regularization factors, $\lambda_{1,2,3}$, is described below. Sensitivity maps were computed using the eigenvector decomposition method

proposed by Lai et al. (22); the temporally averaged, fully sampled center of k-space (averaged temporally) was used for coil calibration. Equation [3] was minimized with a nonlinear conjugate gradient method where the gradient was computed according to (13).

Images were reconstructed in MATLAB on a 12-core Linux workstation with 48 Gb of RAM. Retrospective images were reconstructed as a single 4D problem; prospective images were inverse Fourier transformed in the readout dimension then segmented into blocks of 64 readout points to reduce the memory usage. Reconstruction time was under 30 min for each retrospective image set and approximately 8 h for each prospective set.

Reconstruction Constraints

Equation [3] imposes three l_1 -norm constraints on the data consistency term to suppress incoherent aliasing and synthesize missing data. A 4D decomposition with a Daubechies two wavelet was employed in the spatial and temporal domains. The decomposition level was tailored to the array size to fully compress each dimension of the asymmetric 4D image. A total variation constraint was applied in the spatial domain to attenuate noise and reduce artifacts from the other constraints.

A high-pass filter was applied along the temporal domain to promote a smoothly varying time course. We employed a symmetric window given by [0.06, 0.44, -1, 0.44, 0.06]. This filter was computed by removing the central element from a Gaussian window (FWHM of two points) to remove the weight placed on the current time frame (the data consistency term in Eq. [3] performs this task), normalizing, then subtracting the original signal. This design approach is a variant of the difference of Gaussians method. This filter produces significant coefficients during periods of rapid signal change, which are expected to occur in relatively few voxels, with the largest variation occurring during arrival of the contrast bolus.

The regularization factors λ_1 , λ_2 , and λ_3 were selected to emphasize wavelet sparsity followed by the temporal filter, then total variation. Regularization factors were selected such that the resulting l_1 -norms (scaled by their regularization term) were within a factor of 4 of each other when tested on a subset of the data. This ensured all constraints contributed to the image reconstruction. In the retrospective analysis, the regularization factors were set to $\lambda_1 = 1.0 \times 10^{-4}$, $\lambda_2 = 3.0 \times 10^{-5}$, and $\lambda_3 = 1.5 \times 10^{-3}$; in the prospective study, to $\lambda_1 = 1.5 \times 10^{-3}$, $\lambda_2 = 3.5 \times 10^{-4}$, and $\lambda_3 = 1.5 \times 10^{-2}$.

Retrospective Study

Eight fully sampled DCE data sets were acquired from brain tumor patients. Two sets were discarded due to subject motion; this motion did not compromise the constrained reconstruction, but cases were discarded to ensure that pharmacokinetic modeling parameters represent true signal variations rather than erroneous changes due to misregistration. One case was discarded due to absence of an enhancing lesion. The remaining five sets were retrospectively undersampled then reconstructed to validate the proposed method. Each data set was

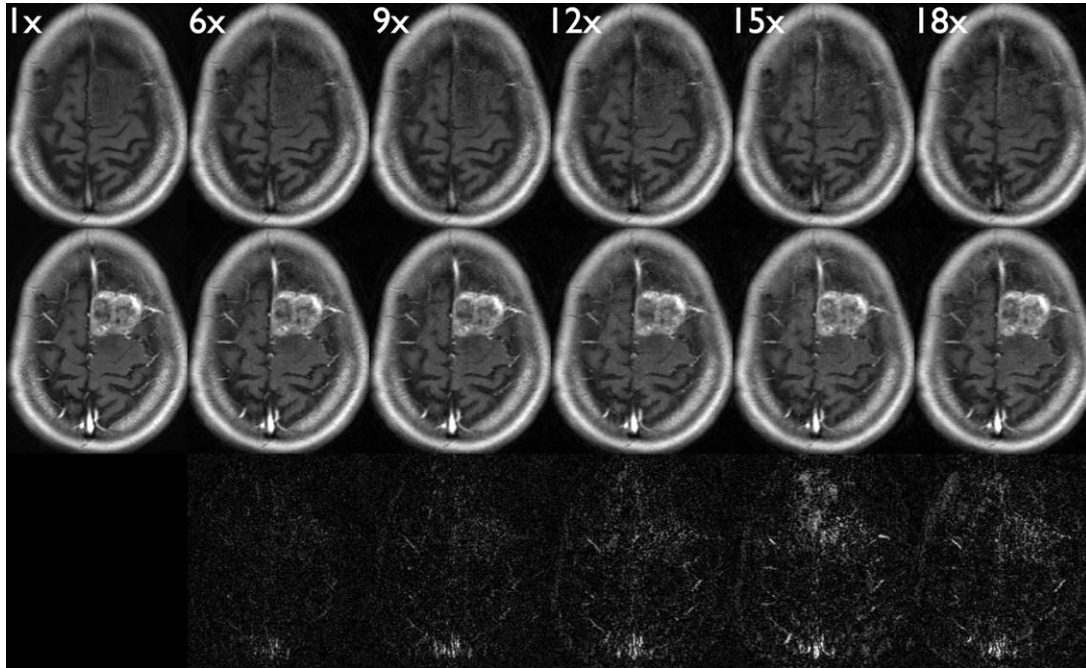


FIG. 2. Representative image quality of retrospectively undersampled data in a patient with a meningioma. A single slice is shown at two adjacent time frames, immediately before (top row) and after (middle row) bolus arrival. The fully sampled case (1 \times) and five acceleration factors (6 \times –18 \times) are presented. High image fidelity is observed at all acceleration rates although increased noise is observed at higher rates, particularly in the enhancing region where substantial signal change occurs between time frames. Difference images (bottom row, intensity scaled by 4 \times) between accelerated and the fully sampled data are shown for images in the middle row. Small vascular regions show the greatest error.

processed twice, with different sampling patterns, effectively doubling the sample size. 3D spoiled gradient echo images were collected on a 3T GE HDxt scanner using an eight-channel head coil with a matrix size of $256 \times 186 \times 10$ and 35 time frames. Spatial resolution was $0.93 \times 1.3 \times 6.0 \text{ mm}^3$; temporal resolution was 10 s.

T_1 -weighting was achieved with a flip angle of 15° and a repetition time of 5.5 ms. Raw data was resampled with variable density Poisson ellipsoid tables at six acceleration factors between 3 \times and 18 \times . A unique sampling table was generated for each reconstruction. In all retrospectively undersampled data, the first time frame

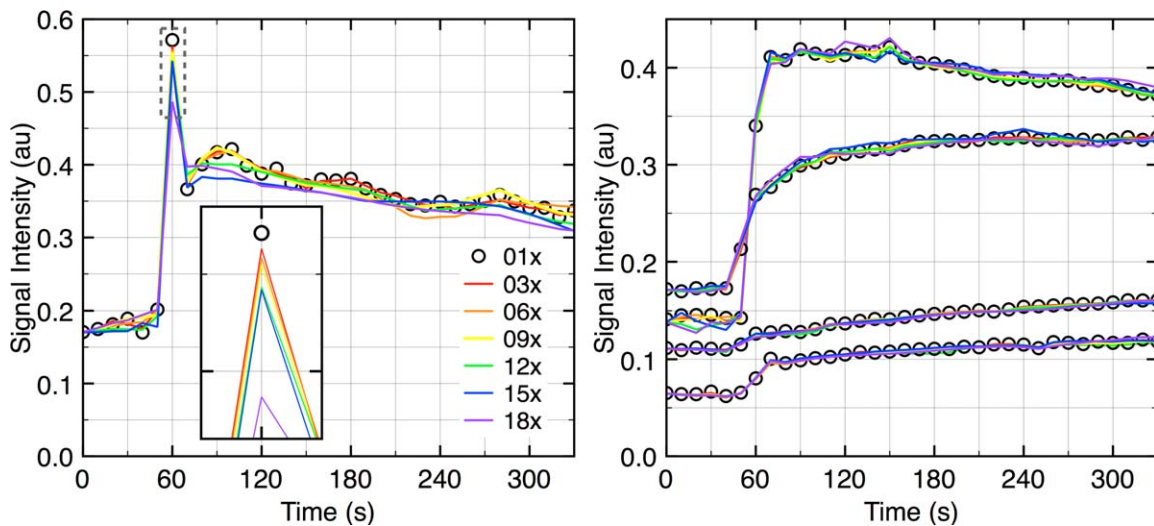


FIG. 3. (left) Typical vascular time-intensity curves for retrospectively undersampled DCE data. A single voxel ROI was selected from a small arteriole near a high contrast boundary. Time-intensity curves from a fully sampled case (open circles) and from six accelerated cases (solid lines) are shown; the region surrounding the bolus arrival is enlarged. High fidelity is maintained, even at 18 \times , although contrast during bolus arrival decreases monotonically with acceleration rate. (right) Fully sampled and accelerated time-intensity curves from multivoxel tumor ROIs in four subjects. Large ROIs and slow signal variation enable near-perfect reconstruction of the contrast dynamics at all acceleration rates. [Color figure can be viewed in the online issue, which is available at wileyonlinelibrary.com]

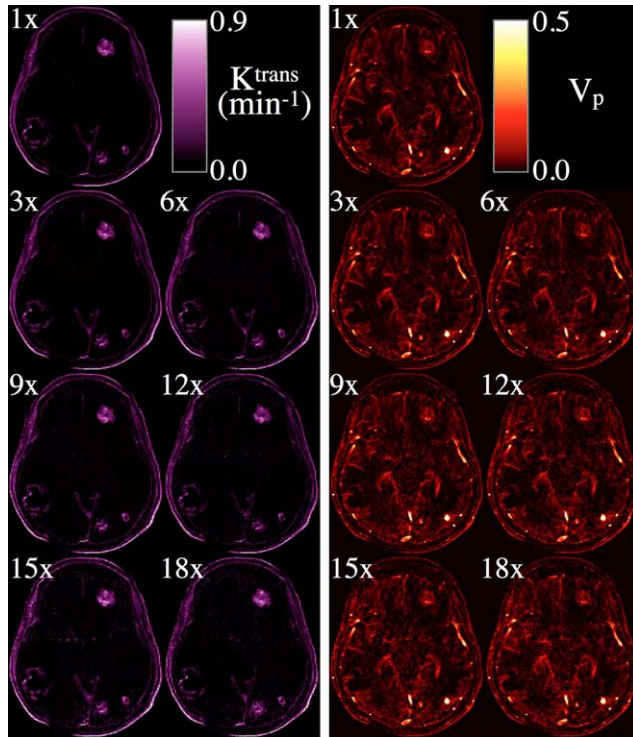


FIG. 4. K^{trans} (left) and v_p (right) maps of a brain tumor patient obtained with fully sampled ($1\times$) and retrospectively undersampled ($3\times$ – $18\times$) images. Parameter values in the tumors remain accurate at all acceleration rates although noise increases with acceleration. [Color figure can be viewed in the online issue, which is available at wileyonlinelibrary.com]

was fully sampled to provide a stable baseline prior to contrast arrival. All subsequent frames were undersampled by the stated rate. Images were reconstructed from Eq. [3].

Typical images are presented for visual assessment and representative time–intensity curves of vascular regions at different acceleration rates are shown. Pharmacokinetic modeling was performed in ImageJ with TOPPCAT (23) to obtain the volume transfer constant between plasma and the extravascular-extracellular space (K^{trans} , units of min^{-1}) and the fractional plasma volume (v_p , unitless) maps. The AIF was selected from a small arterial region-of-interest (ROI; between 1 and 4 voxels). The same ROI was used at all acceleration rates but the plasma concentration was measured from the correspondingly sampled image, and so varied with acceleration rate. The baseline longitudinal relaxation time was assumed to be 1.0 s for all pharmacokinetic modeling. This isolates errors related to acceleration and constrained reconstruction—the objective of this work—at the expense of absolute quantitation.

Prospective Study

Ten prospectively undersampled data sets were acquired from multiple sclerosis patients and from brain tumor patients. Two data sets were discarded due to subject motion that hindered pharmacokinetic modeling; undersampled reconstruction was not substantially compromised due to this motion. Coronal 3D spoiled gradient echo images were acquired with a flip angle of 15° and a repetition time of 4.5 ms. The acquisition matrix was $256 \times 256 \times 128$ with 82 time frames, corresponding to a spatial resolution of $0.94 \times 0.94 \times 1.9 \text{ mm}^3$ and a temporal resolution of 4.1 s. The net acceleration factor was $36\times$. The same variable density Poisson ellipsoid sampling table was used for all subjects. The contrast injection occurred 45 s into the scan to provide stable baseline images; the first five image volumes (~ 20 s) were discarded.

Images were evaluated qualitatively for aliasing artifacts and spatial-temporal blurring. Time–intensity

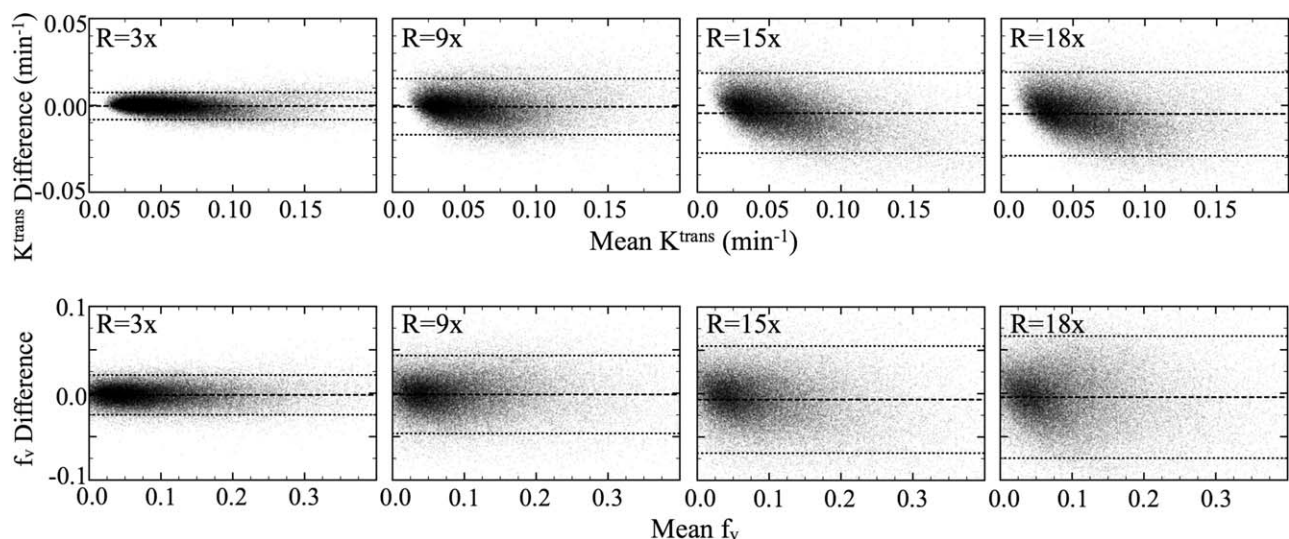


FIG. 5. Bland–Altman plots showing differences between fully sampled and accelerated parameters versus their average. Average differences are indicated with dashed lines; ± 1.96 standard deviations with dotted lines. Mean differences are all near zero but the width of the standard deviation bars increases with acceleration. Also visible is a trend toward overestimation of accelerated K^{trans} with increasing permeability—this is attributed to contrast attenuation of the AIF at high acceleration rates, similar to Figure 3 (left). Acceleration rates of $6\times$ and $12\times$ have been omitted for clarity; they demonstrate the same trend observed in the rates shown.

Table 1
Linear Regression Parameters Relating Pharmacokinetic Modeling Outputs Obtained from Retrospectively Undersampled to Fully Sampled Images

Acceleration rate	K^{trans}			v_p		
	Slope	Intercept	R^2	Slope	Intercept	R^2
3×	1.001	0.0003	0.99	0.991	0.0027	0.98
6×	1.078	-0.0036	0.96	0.985	0.0060	0.95
9×	0.972	0.0025	0.95	0.971	0.0041	0.93
12×	0.980	0.0016	0.92	0.953	0.0116	0.88
15×	1.095	-0.0013	0.92	1.019	0.0051	0.88
18×	1.033	0.0030	0.90	0.983	0.0061	0.84

curves from vascular ROIs (between 1–5 voxels) were analyzed and compared to fully sampled data sets from subjects included in the retrospective study.

Pharmacokinetic modeling was performed with TOPPCAT (23) to obtain K^{trans} and v_p . Like in the retrospective study, a small arterial ROI was used to measure the AIF. The baseline longitudinal relaxation time was again assumed to be 1.0 s. This was done for two reasons: first, we are only concerned with acceleration-induced variations. Second, acquiring accurate T_1 maps becomes challenging with this high resolution DCE scan: T_1 mapping can take longer than the dynamic scan and optimization of this process is beyond the scope of this work. Lack of baseline T_1 values precludes truly quantitative modeling; implications are discussed below.

The nasal turbinate mucosa served as a reference tissue to validate the accuracy of the prospectively accelerated DCE protocol. Average permeability and plasma volume fractions were obtained from ROIs in the eight prospectively accelerated scans (number of voxels per ROI: average, 312; range, 94–653) and from a cohort of eight fully sampled scans (number of voxels per ROI: average, 420; range, 169–924), drawn from a clinical database based on appropriate slice coverage. A two-tailed paired t -test was employed to probe for differences between accelerated and fully sampled parameters.

RESULTS

Retrospective Study

Figure 2 contains a single slice at two adjacent time points from a meningioma patient reconstructed from the same source data but retrospectively undersampled to simulate different acceleration rates (as labeled). No residual aliasing artifacts are seen but increased noise is observed as the acceleration factor is increased from 1× (fully sampled) to 18×. Loss of spatial resolution is visible with increasing acceleration factor, as evidenced by blurring of small vascular features. Difference images between the fully sampled and accelerated images during maximal vascular enhancement report negligible temporal blurring of the contrast dynamics in the large tumor region. Small vascular regions are the most prominent features in these difference images, suggesting some signal attenuation as the contrast bolus arrives.

Representative time-intensity curves from an arterial ROI at various acceleration factors are shown in Figure 3a. A single voxel ROI in a small artery near high contrast boundaries was selected since similar regions were identified on subtraction images, as noted above. Multivoxel ROIs and larger vascular structures frequently provide improved fidelity (not shown). Accelerated curves show no premature contrast arrival or delayed washout; however, a monotonic decrease in signal intensity with increasing acceleration rate is observed at maximum enhancement, as shown in the subplot. Time-intensity curves from multivoxel tumor ROIs (over 100 voxels per ROI) in four subjects are shown in Figure 3b. Regional averaging from the large ROIs and relatively slow signal variation enables accurate reproduction of the contrast dynamics at all acceleration factors investigated. Overall, exceptional fidelity was observed in the contrast dynamics considering the small matrix size (only 186×10 phase- and slice-encodes) and the high acceleration rates considered.

Typical K^{trans} and v_p maps obtained with fully sampled and retrospectively undersampled data are shown in Figure 4. Parameter maps appear stable as the acceleration rate is increased. In all cases, regions with high permeability can be readily discerned and the

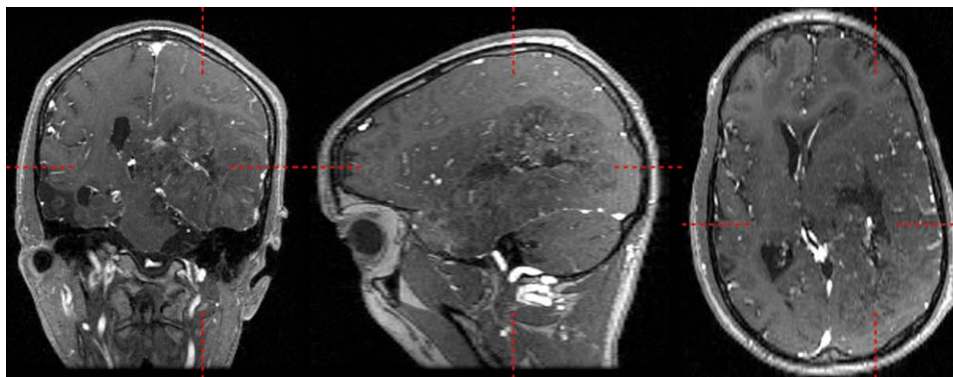


FIG. 6. Representative raw images acquired with a 36× acceleration. Images were acquired coronally, but thin slices enable effective axial and sagittal reformats. Full brain coverage with high spatial resolution ensures acquisition of the entire brain tumor and potential metastases and enables reliable sampling of the AIF since numerous arterial and venous structures are readily visible. Slice locations are indicated with dashed lines. [Color figure can be viewed in the online issue, which is available at wileyonlinelibrary.com]

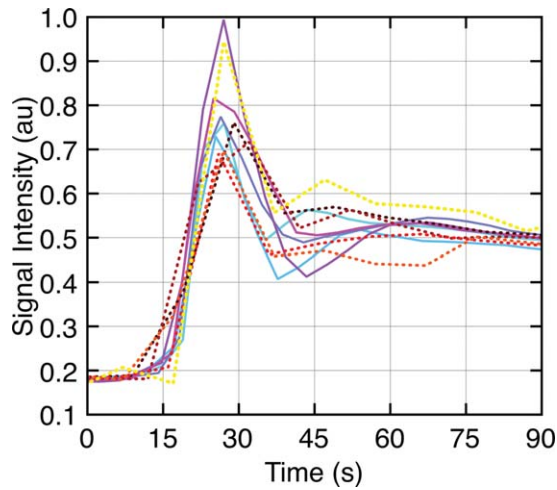


FIG. 7. Vascular time-intensity curves from 10 different subjects. Five 36 \times -accelerated scans are shown with solid lines and cool colors (blue/purple); five fully sampled scans are represented with dotted lines and hot colors (red/yellow). Contrast dynamics of the accelerated scans are consistent with fully sampled data: no premature contrast arrival or washout is observed, maximum enhancement appears unaffected, and intrasubject variability is equal to, or reduced, in accelerated relative to fully sampled images.

fractional plasma volume is consistent at all acceleration rates. Subtle features remain preserved in both parameters despite the slight loss of resolution in the source images (presented above in relation to Fig. 2). Noise amplification is observed with increased acceleration, particularly in v_p , but expected given the vast amount of discarded data.

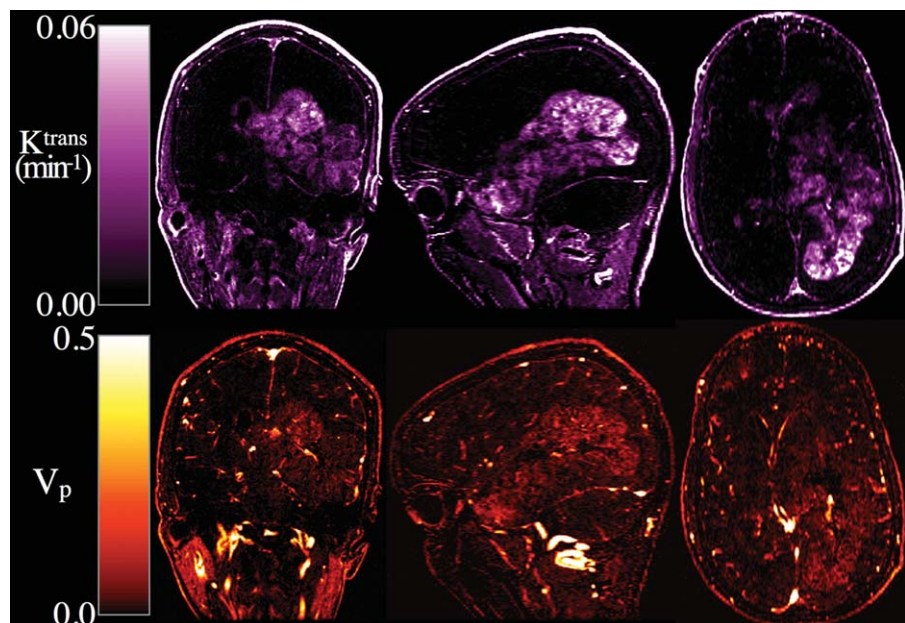
Bland-Altman plots in Figure 5 and linear regression parameters in Table 1 indicate that the proposed sampling scheme and reconstruction method can be employed for accurate pharmacokinetic modeling. Slopes (see Table 1) relating accelerated to fully sampled

parameters deviate by less than 10% and no divergence is observed as the acceleration rate is increased. The most substantial mean difference reported in the Bland-Altman plots for K^{trans} is -0.0049 min^{-1} and occurs with 18-fold acceleration. Increased variance in the parameter maps is the primary effect of acceleration with retrospective data: the R^2 values in Table 1 decrease and the standard deviation bars in Figure 5 widen with increasing acceleration rate. This is consistent with the images shown in Figure 4 where overall map appearance remains constant at all acceleration rates, but noise is amplified. The Bland-Altman plots report a rate dependent overestimation in K^{trans} (N.B., values are overestimated when the difference is negative). This bias occurs more strongly at high acceleration rates than at lower rates: it is negligible at rates up to, and including, 12 \times , and never exceeds 10% overestimation at 15 \times and 18 \times . This is caused by signal attenuation in the AIF (Fig. 3) and is discussed below. No bias was observed in v_p . We conclude that acceleration and constrained reconstruction can provide highly accurate pharmacokinetic modeling, irrespective of the acceleration rate but is limited by the signal-to-noise ratio.

Prospective Study

Figure 6 contains representative images reconstructed from highly accelerated data during maximal vascular signal enhancement. These images represent a considerable improvement relative to our center's typical DCE protocol: voxel volume is reduced by 4.5 \times , slice coverage is improved by 33 \times , and temporal resolution is reduced by 1.2 \times . Thin slices enable effective multiplanar reformats and full brain coverage ensures that the entire pathology is acquired. Images—particularly the axial reformat, revealing both phase-encode dimensions—show no residual aliasing artifact and features of similar size to the acquired resolution are visible. Signal-to-noise

FIG. 8. Permeability and fractional plasma volume maps from a glioblastoma multiforme patient obtained with the 36 \times accelerated DCE protocol (raw images in Figure 6). Thin slices permit axial and sagittal reformats. High resolution maps allow for detailed visualization of the tumor structure and full brain coverage ensures that the entire tumor is quantified.



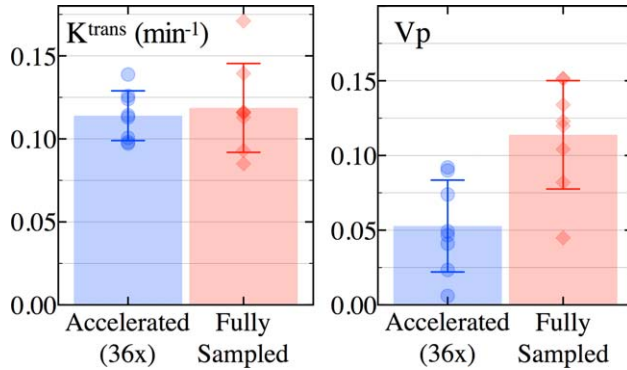


FIG. 9. K^{trans} (left) and v_p (right) values measured in the nasal mucosa of sixteen patients using prospectively accelerated (blue, circles) and fully sampled DCE images (red, diamonds). K^{trans} values did not differ significantly between groups. A significant difference was observed in v_p ; this was attributed to partial volume effects in the fully sampled case between tissue and the surrounding vasculature, which inflates v_p . [Color figure can be viewed in the online issue, which is available at [wileyonlinelibrary.com](http://www.wileyonlinelibrary.com)]

ratio, although difficult to quantify, remains adequate to perform pharmacokinetic modeling.

Vascular time–intensity curves from five prospectively accelerated images, chosen randomly from our cohort of eight, and from five fully sampled images from different patients are presented in Figure 7. Curves were time-shifted and intensity scaled to account for different injection delays, transit times, concentrations, and image scaling. Comparison of these curves suggests that the contrast dynamics are being accurately detected: no premature arrival or delayed washout is observed in the accelerated cases. The average peak signal enhancement is slightly greater in the accelerated case than in the fully sampled data, likely due to a combination of improved temporal resolution and reduced partial volume effects.

Permeability and plasma fraction maps are shown in Figure 8 for a glioblastoma multiforme patient acquired with the 36 \times accelerated protocol (raw images in Fig. 6). Permeability maps appear as expected: vascular leakage is confined to the tumor and to tissues lacking the blood brain barrier (such as the meninges and muscle). No leakage is observed in the healthy parenchyma. Fine detail, comparable to the acquired resolution, can be seen within the tumor on K^{trans} maps. v_p maps show elevated vascularity within the tumor and correlate with tumor permeability. The noise level in the v_p maps indicates this protocol is near the signal-to-noise ratio limit for pharmacokinetic modeling.

Accuracy of prospectively accelerated K^{trans} and v_p are presented in Figure 9. Individual data points represent average values from nasal turbinate mucosa ROIs of subjects imaged with either the accelerated or the standard protocol. Intersubject averages are reported with the filled boxes; error bars indicate ± 1 standard deviation. No significant K^{trans} difference ($P=0.67$) was observed between groups. The accelerated protocol had a standard deviation that was 56% of the fully sampled protocol's. This is attributed to more reliable ROI placement in the accelerated case rather than fundamentally reduced

variance. A significant difference ($P=0.003$) in plasma fraction was observed between groups. This bias is attributed to partial volume averaging between nasal turbinate mucosa tissue and surrounding vasculature that increases the apparent plasma fraction of the fully sampled cases; high resolution diminished this effect in the accelerated protocol.

DISCUSSION

The objective here was to develop and validate an accelerated method for dynamic imaging applied to DCE MRI. We invented a sampling scheme that enables combined PI and CS for dynamic applications and proposed reconstruction constraints that provide accurate image reconstruction. This method was validated with a retrospective analysis of fully sampled data and with prospectively accelerated data.

Data was acquired according to a novel variable density Poisson ellipsoid scheme. This approach defines a set of sampling locations that balance random sampling with uniform spacing and incorporates increased density in the center of k-space. This approach is compatible with various array coil geometries and matrix sizes making it flexible and robust; however, computation time (typically about 5–120 s per dynamic table) favors pre-computation over real-time construction. Alternate sampling strategies, such as Cartesian radial (24,25) may also prove effective for DCE imaging.

We opted to include multiple reconstruction constraints, including a 4D wavelet, temporal filtering, and spatial finite differences. We anticipate complementary behavior from these constraints: the temporal filter promotes a smoothly varying time-course, but is voxel-independent. The wavelet transform provides both temporal and spatial compression, but imposes edge artifacts. The total variation constraint partially attenuates these edge artifacts and promotes a smoothly varying image. Regularization factors were selected empirically and, admittedly, limit direct reproduction of this work. Future efforts should be directed to automatically tune such variables.

Image Quality

The retrospective study simulated acceleration rates between 3 \times and 18 \times and proved to be challenging. These rates are substantial given the small matrix size: only 104 encodes remain in each time frame at 18 \times . Thin axial slabs obstruct PI efficacy in the slice-encode direction, effectively offloading the reconstruction burden to the CS sparsity constraints. Despite these challenges, exceptional image quality is observed, Figure 2. The most severely affected regions are small blood vessels, further illustrated in Figure 3a. These small structures are most vulnerable to distortion from the spatial-temporal constraints since their contrast is encoded into the periphery of k-space, which is sampled least densely.

Although 18 \times was the maximum acceleration considered retrospectively, this rate does not translate directly to prospectively undersampled data. Prospective images were acquired in the coronal plane to leverage the

receive coil geometry for 2D PI. This, combined with much higher matrix sizes than the retrospective study, justified the $36\times$ acceleration rate employed in this work. Each time frame contained 912 samples, and new frames occurred $\sim 2.5\times$ more frequently than the retrospective study. Relative to the $18\times$ retrospective data, prospective cases had $\sim 21\times$ more data per unit time; direct extrapolation of retrospective results to the prospective case is misleading.

In the prospective study, acceleration was used to acquire high resolution images with full brain coverage. This strategy rapidly depletes the signal-to-noise ratio while requiring more samples for volume encoding; higher acceleration rates are likely possible if lower spatial and higher temporal resolution are prescribed. Despite low signal-to-noise ratio, anatomical features are clearly discernable in the prospective images, Figure 6; furthermore, temporal signal degradation was not detected, Figure 7, which bodes well for accurate pharmacokinetic modeling, Figures 8 and 9.

Accuracy

This study aimed to quantify acceleration-induced errors in pharmacokinetic modeling parameters. Retrospective analysis provides a convenient gold standard but is limited by small matrix sizes (186 phase-encodes, 10 slice-encodes, and 35 time frames) and a temporal resolution (10 s) that fails to resolve all dynamic features. Furthermore, subsampling a fully sampled data set fails to improve the temporal resolution. Prospective acceleration enables large array sizes and/or high temporal resolution but lacks an intrinsic reference. Both studies suggest that pharmacokinetic modeling remains accurate at high acceleration factors. The signal-to-noise ratio and distortion of the AIF are two limiting factors to consider when designing accelerated DCE protocols.

Our retrospective analysis reports both over- and underestimation of K^{trans} with no diverging trend as the acceleration rate is increased, Table 1. Bland–Altman plots, Figure 5, confirm that no bulk bias is present. As with conventional PI, noise remains the primary limiting factor. Bland–Altman plots indicate slight ($<10\%$) rate dependent K^{trans} errors at high acceleration. This bias results from temporal distortions of small vascular structures, which were used to define AIFs for pharmacokinetic modeling, during bolus arrival, Figure 3a (inset). Signal attenuation during maximal enhancement causes a temporary underestimation of the contrast agent in the plasma. Rapidly enhancing tissues show substantial signal changes during this period but are less attenuated by the acceleration/constrained reconstruction than the AIF, Figure 3. This results in a rate dependent exaggerated permeability. We believe, although have not verified, that this trend would be reduced or eliminated if larger vascular structures (these were not reliably available with the retrospective data) or population derived AIFs are employed.

To date, few studies have reported the accuracy of CS-accelerated DCE imaging. Smith et al. (16,17) report accurate pharmacokinetic modeling at low acceleration rates although show considerable K^{trans} underestimation in human data and overestimation in mouse data. Chen

et al. (15) report very slight underestimation of K^{trans} and k_{ep} but do not employ a patient specific AIF, where we observed the greatest potential for bias. Han et al. (18) performed a retrospective and prospective analysis of 2D DCE imaging. They report a concordance correlation coefficient of 0.83 ± 0.11 (mean \pm s.d.) at $8\times$ acceleration, although it is unclear if this represents a loss of accuracy or of precision. Together, existing literature and the present study suggest that CS and PI are viable techniques for accurate DCE imaging.

Limitations

There are numerous limitations of this study that could not be addressed succinctly in this manuscript. Considerable analysis hinged on visual assessment of image quality. Raw images, time–intensity curves, and parameter maps were presented for qualitative appraisal and regularization parameters in Eq. [3] were tuned empirically based on image appearance. Although suboptimal, quantitative metrics for image quality are not yet available for CS reconstructed images and simple metrics, like mean squared error or signal-to-noise, are not indicative of actual image quality. In all cases, typical data and image quality was presented.

Validation of the proposed method was performed with a retrospective analysis of fully sampled data and with a comparison between a cohort of prospectively accelerated patient scans and a separate population of fully sampled data. Both approaches have limitations and improved validation should be performed. A case control study involving fully sampled and prospectively accelerated scans in the same patient would reduce intersubject variability and more fully characterize the accuracy and precision of this method.

Numerous software packages exist for DCE modeling and substantial variation in image processing, modeling, and fitting routines exist. We employed TOPPCAT (23), a freely available package. This software performs no image processing, as desired to isolate acceleration and reconstruction errors, and extracts the AIF from a user defined ROI placed on the raw DCE images. This package does not estimate v_e , the extravascular-extracellular space, a standard output in DCE modeling (2). Inclusion of this parameter is desirable, but was not available.

Modeling inputs were observed to generate variations in K^{trans} and v_p that exceed acceleration-induced errors. Permeability and plasma volume were particularly sensitive to the AIF; considerable effort was invested in careful and consistent selection of the region defining the AIF.

Truly quantitative modeling requires baseline tissue T_1 values (1,9). Throughout this work, we assumed a T_1 value of 1.0 s. This prevents absolute quantitation, but does not compromise our findings, which demonstrate that acceleration and constrained reconstruction are compatible with permeability modeling. Although not shown, a fully sampled case was reprocessed assuming T_1 values of 0.8, 1.0, and 1.2 s. Average K^{trans} in an enhancing tumor differed by less than 0.4%; v_p by 1.7%; R^2 by 0.03%.

Current reconstruction times (~8 h) preclude real-time assessment or modeling. Although the reconstruction is iterative, all sparsity transforms and operations are highly parallelizable; additional parallel computing—via GPGPU's or distributed computers—may vastly reduce the reconstruction time.

CONCLUSION

We have invented a sampling and reconstruction technique for highly accelerated dynamic MRI using PI and CS. This method was shown to provide accurate DCE permeability imaging: double-digit acceleration factors are readily achievable without loss of accuracy in K^{trans} or v_p . This approach enables large field-of-view DCE imaging with high spatial-temporal resolution.

REFERENCES

- Tofts PS, Kermode AG. Measurement of the blood-brain barrier permeability and leakage space using dynamic MR imaging. 1. Fundamental concepts. *Magn Reson Med* 1991;17:357–367.
- Tofts PS, Brix G, Buckley DL, et al. Estimating kinetic parameters from dynamic contrast-enhanced T(1)-weighted MRI of a diffusable tracer: standardized quantities and symbols. *J Magn Reson Imaging* 1999;10:223–232.
- Mills SJ, Patankar TA, Haroon HA, Baleriaux D, Swindell R, Jackson A. Do cerebral blood volume and contrast transfer coefficient predict prognosis in human glioma? *AJNR Am J Neuroradiol* 2006;27:853–858.
- Batchelor TT, Sorensen AG, di Tomaso E, et al. AZD2171, a pan-VEGF receptor tyrosine kinase inhibitor, normalizes tumor vasculature and alleviates edema in glioblastoma patients. *Cancer Cell* 2007;11:83–95.
- O'Connor JP, Jackson A, Parker GJ, Jayson GC. DCE-MRI biomarkers in the clinical evaluation of antiangiogenic and vascular disrupting agents. *Br J Cancer* 2007;96:189–195.
- Kershaw LE, Cheng HL. Temporal resolution and SNR requirements for accurate DCE-MRI data analysis using the AATH model. *Magn Reson Med* 2010;64:1772–1780.
- Planey CR, Welch EB, Xu L, et al. Temporal sampling requirements for reference region modeling of DCE-MRI data in human breast cancer. *J Magn Reson Imaging* 2009;30:121–134.
- Yankeelov TE, Gore JC. Dynamic contrast enhanced magnetic resonance imaging in oncology: theory, data acquisition, analysis, and examples. *Curr Med Imaging Rev* 2009;3:91–107.
- Evelhoch JL. Key factors in the acquisition of contrast kinetic data for oncology. *J Magn Reson Imaging* 1999;10:254–259.
- Paldino MJ, Barboriak DP. Fundamentals of quantitative dynamic contrast-enhanced MR imaging. *Magn Reson Imaging Clin North Am* 2009;17:277–289.
- Korosec FR, Frayne R, Grist TM, Mistretta CA. Time-resolved contrast-enhanced 3D MR angiography. *Magn Reson Med* 1996;36:345–351.
- Tudorica LA, Oh KY, Roy N, et al. A feasible high spatiotemporal resolution breast DCE-MRI protocol for clinical settings. *Magn Reson Imaging* 2012;30:1257–1267.
- Lustig M, Donoho D, Pauly JM. Sparse MRI: the application of compressed sensing for rapid MR imaging. *Magn Reson Med* 2007;58:1182–1195.
- Adluru G, Tasdizen T, Schabel MC, DiBella EV. Reconstruction of 3D dynamic contrast-enhanced magnetic resonance imaging using nonlocal means. *J Magn Reson Imaging* 2010;32:1217–1227.
- Chen L, Schabel MC, DiBella EV. Reconstruction of dynamic contrast enhanced magnetic resonance imaging of the breast with temporal constraints. *Magn Reson Imaging* 2010;28:637–645.
- Smith DS, Welch EB, Li X, Arlinghaus LR, Loveless ME, Koyama T, Gore JC, Yankeelov TE. Quantitative effects of using compressed sensing in dynamic contrast enhanced MRI. *Phys Med Biol* 2011;56:4933–4946.
- Smith DS, Li X, Gambrell JV, Arlinghaus LR, Quarles CC, Yankeelov TE, Welch EB. Robustness of quantitative compressive sensing MRI: the effect of random undersampling patterns on derived parameters for DCE- and DSC-MRI. *IEEE Trans Med Imaging* 2012;31:504–511.
- Han S, Paulsen JL, Zhu G, Song Y, Chun S, Cho G, Ackerstaff E, Koutcher JA, Cho H. Temporal/spatial resolution improvement of in vivo DCE-MRI with compressed sensing-optimized FLASH. *Magn Reson Imaging* 2012;30:741–752.
- Lustig M, Alley M, Vasanawala S, Donoho D, Pauly J. L1 SPIR-iT: autocalibrating Parallel Imaging Compressed Sensing. In Proceedings of the 17th Annual Meeting of ISMRM, Honolulu, Hawaii, USA, 2009. p 379.
- Bo L, Yi MZ, Ying L. Sparsesense: application of compressed sensing in parallel MRI. *International Conference on Information Technology and Applications in Biomedicine*, 2008. p 127–130.
- King K. Combining compressed sensing and parallel imaging. In Proceedings 16th Annual Meeting of ISMRM, Toronto, Canada, 2008. p 1488.
- Lai P, Lustig M, Brau AC, Vasanawala S, Beatty PJ, Alley M. Efficient L1SPIRiT reconstruction (ESPIRiT) for highly accelerated 3D volumetric MRI with parallel imaging and compressed sensing. In Proceedings of the 18th Annual Meeting of ISMRM, Stockholm, Sweden, 2010. p. 345.
- Barboriak DP, MacFall JR, Padua AO, York GE, Vigiante BL, Dewhirst MW. Standardized software for calculation of K^{trans} and v_p from dynamic T1-weighted MR images. In Proceedings of the ISMRM Workshop on MR in Drug Development: from Discovery to Clinical Therapeutic Trials, McLean, Virginia, USA, 2004.
- Chan RW, Ramsay EA, Cheung EY, Plewes DB. The influence of radial undersampling schemes on compressed sensing reconstruction in breast MRI. *Magn Reson Med* 2012;67:363–377.
- Prieto C, Uribe S, Razavi R, Atkinson D, Schaeffter T. 3D undersampled golden-radial phase encoding for DCE-MRA using inherently regularized iterative SENSE. *Magn Reson Med* 2010;64:514–526.